Current Optics and Photonics
Vol. 1, No. 4, August 2017, pp. 402-411

ISSN: 2508-7266(Print) / ISSN: 2508-7274(Online)
DOI: https://doi.org/10.3807/COPP.2017.1.4.402

A Novel Classification of Polymorphs Using Combined LIBS and Raman Spectroscopy

Dongwoo Han, Daehyoung Kim, Soojin Choi, and Jack J. Yoh*

Department of Mechanical and Aerospace Engineering, Seoul National University, Seoul 08826, Korea

(Received January 31, 2017 : revised June 6, 2017 : accepted June 7, 2017)

Combined LIBS-Raman spectroscopy has been widely studied, due to its complementary capabilities as an elemental analyzer that can acquire signals of atoms, ions, and molecules. In this study, the classification of polymorphs was performed by laser-induced breakdown spectroscopy (LIBS) to overcome the limitation in molecular analysis; the results were verified by Raman spectroscopy. LIBS signals of the $CaCO_3$ polymorphs calcite and aragonite, and $CaSO_4 \cdot 2H_2O$ (gypsum) and $CaSO_4$ (anhydrite), were acquired using a Nd:YAG laser (532 nm, 6 ns). While the molecular study was performed using Raman spectroscopy, LIBS could also provide sufficient key data for classifying samples containing different molecular densities and structures, using the peculiar signal ratio of 5s → 4p for the orbital transition of two polymorphs that contain Ca. The basic principle was analyzed by electronic motion in plasma and electronic transition in atoms or ions. The key factors for the classification of polymorphs were the different electron quantities in the unit-cell volume of each sample, and the selection rule in electric-dipole transitions. The present work has extended the capabilities of LIBS in molecular analysis, as well as in atomic and ionic analysis.

Keywords : Laser-induced breakdown spectroscopy (LIBS), Raman spectroscopy, Polymorphs, Orbital transition, Selection rule
OCIS codes : (300.0300) Spectroscopy; (140.3440) Laser-induced breakdown; (140.3550) Lasers, Raman; (280.5395) Plasma diagnostics

I. INTRODUCTION

Laser-induced breakdown spectroscopy (LIBS) and Raman spectroscopy are widely used in various fields as composition analyzers. They share the common advantages of not requiring sample preparation, having rapid signal acquisition, and being useful for standoff detection. Raman spectroscopy focuses on the Raman-scattering signal, which is caused by the vibrational, rotational, and other frequency modes of molecules [1, 2]. In contrast, LIBS is used to analyze atomic and ionic information by receiving signals from plasma. Therefore, the two techniques have been used together, as they provide complementary information. In addition, they can share many optical components, such as the lens, mirror, and even the laser or spectrometer.

On the other hand, the required laser energy and optimal detection time for LIBS and Raman differ. Generally, LIBS and Raman spectroscopy for elemental analysis have been conducted individually. First, LIBS has been well utilized for the purposes of archeology, explosive materials, and space exploration, in that it provides atomic or ionic information [3-5]. On the other hand, Raman spectroscopy has mainly been used for qualitative analysis in classifying polymorphs or other mixed molecular compositions. For example, Rull *et al*. attempted to investigate molecular compositions based on Ca, Si, and Fe in some meteorites using Raman spectroscopy [6]. Wang *et al*. analyzed various magnesium sulfates containing different quantities of H_2O molecules, for Mars exploration [7]. Hemley analyzed the shifts of Raman spectra following changes in molecular density due to high pressure, using SiO_2 polymorphs [8].

Many researchers have also performed combined LIBS

*Corresponding author: jjyoh@snu.ac.kr
Color versions of one or more of the figures in this paper are available online.

and Raman studies to obtain the complementary information from atoms, ions, and molecules [9-11]. Furthermore, some attempts have even been made to simultaneously obtain LIBS and Raman signals, to combine their individual benefits [12-14].

Until now, analysis of polymorphs was not possible using LIBS because LIBS spectra generally do not provide information about molecular structure. However, in the present study the classification of polymorphs using LIBS was performed by comparing signal intensities from LIBS spectra. When comparing LIBS signals from two calcium-containing polymorphs, the signal ratio of the emission lines associated with the $5s \rightarrow 4p$ orbital transition were found to have a peculiarity: The signal intensity of the $5s \rightarrow 4p$ transition does not change much, even though the intensities for two polymorphs show a difference, due to the electrons in the plasma and the transition process in atoms. Therefore, by comparing the signal ratios of the $5s \rightarrow 4p$ orbital transition to other transitions, we can classify two polymorphs, as they contain different quantities of the main elements in their unit-cell volumes.

Ca-based polymorphs ($CaCO_3$) were used because Ca-rich minerals are abundant not only on Earth but also on the moon and Mars, and are frequently targeted in space investigation, as well as in analysis of pigments and historical antiques [9, 10, 15]. Also, orbital information for Ca helps to investigate metal-poor stars in astronomy quantitatively [16, 17]. In addition, experiments for measuring the lifetimes of metastable states have been conducted for some time [18-20]. This broad utilization of Ca provides deep information on its microscopic orbital and transition processes. In addition, this abundant information on Ca significantly helps us to set a standard, specific wavelength range that classifies polymorphs in LIBS. We therefore attempted to obtain and compare LIBS spectra of two $CaCO_3$ polymorphs (calcite and aragonite), and of $CaSO_4 \cdot 2H_2O$ (gypsum) and $CaSO_4$ (anhydrite).

This study aims to maximize the complementary utilization of a combined LIBS-Raman system, whereby the information obtained by classifying polymorphs using LIBS can be reexamined by Raman spectroscopy, thus improving the accuracy and reliability of elemental analysis using the combined system.

II. EXPERIMENTAL SETUP

Figure 1 shows the schematic diagram of the LIBS and Raman setup. The Q-switched Nd:YAG laser (Surelite I, Continuum, 532 nm, 6 ns pulse duration) was used to generate laser-induced plasma and Raman scattering. The laser beam was focused using a BK-7 plano-convex lens (2 inch diameter, 90 mm focal length) onto samples of $CaCO_3$ (calcite, aragonite) and $CaSO_4 \cdot 2H_2O$ (gypsum) and $CaSO_4$ (anhydrite), obtained from Hansol Education Co. (hs-97-2001). Samples were analyzed without any processing.

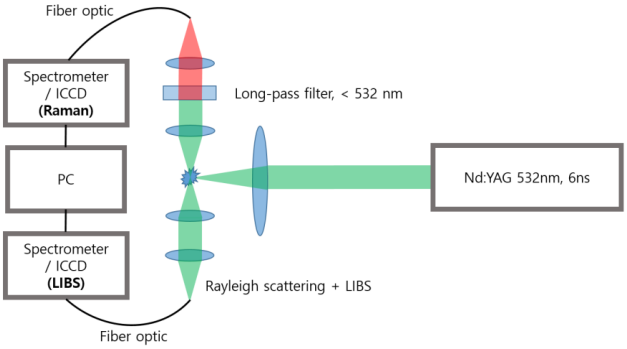

FIG. 1. Schematic diagram of the experiment.

In addition, the samples were fixed to an *xyz*-axis stage.

A laser energy of 40 mJ/pulse (1.7 GW/cm^2) was used to make enough plasma to obtain a LIBS signal, which is generated after sample ablation. The LIBS plasma was generated after collimation using two BK-7 plano-convex lenses (2 inch diameter, 100 mm focal length). LIBS spectra were collected using an ICCD (Andor Mechelle ME5000 Echelle), which covers a wavelength range of about 200 nm to 975 nm. Gate delay was set at 1 μs, and the gate width was 20 μs. The laser beam was fired at five locations, with 10 shots for each location. The first five shots were discarded, to remove surface impurities.

For the Raman spectroscopy, a laser energy of 20 mJ/pulse (0.87 GW/cm^2) was used. The Raman-scattering signal was also focused after being collimated by two BK-7 plano-convex lenses (2 inch diameter, 100 mm focal length), and the collimated light passed through a long-pass filter with a transition width of 186 cm^{-1} (532 nm, LP03-532RU-25), to eliminate strong Rayleigh-scattered light. The filtered light was focused on an optical fiber and passed through the diffraction grating in the Raman spectrometer (MonoRa 320i, 320 mm focal length). To obtain a clear signal, the grating mode (1200 groove/mm or 600 groove/mm, 500 nm blaze) was selected to be 1200 groove/mm, which shows Raman signals in the 0-4000 cm^{-1} wave number range in one laser shot. The Raman spectra were also captured, by a Raman ICCD (Andor iStar DH734-18F-03). The gate delay of the Raman ICCD was set at 0 ns, since Raman scattering occurs immediately after the laser beam irradiates the sample. The gate width was varied from 0.1 μs to 1 μs, to find a clear signal and to minimize the influence of fluorescence. In addition, the exposure time of the ICCD was 0.1 s and the gain was set at 3000, to obtain weak Raman signals. Raman data from 20 pulses were accumulated.

The Raman and LIBS spectrometers were synchronized with the Q-switched Nd:YAG laser using a pulse generator (BNC-565-8CG). An oscilloscope (Tektronix TDS-2014) was applied to obtain precise timing of input and output signals, which helps with synchronization between the laser and pulse generator.

III. RESULTS AND DISCUSSION

3.1. $CaCO_3$ Polymorphs

Figure 2 shows the Raman signals for the $CaCO_3$ polymorphs calcite and aragonite. The internal vibrational mode of the CO_3^{2-} is detected at around 1080 cm^{-1} in both samples. However, near the 100-400 cm^{-1} range, the two polymorphs showed different peaks. Aragonite signals were seen at 230 cm^{-1} and 260 cm^{-1}, whereas the calcite signal emerged at 380 cm^{-1}. The signal differences are caused by the different vibrational modes of Ca^{2+} and CO_3^{2-}, due to the bond lengths in the molecules. For calcite, the interatomic distance between Ca^{2+} and CO_3^{2-} is greater than that of aragonite; therefore, aragonite is formed with a stronger bond, whereas calcite has a weaker bond between Ca^{2+} and CO_3^{2-}. Thus calcite showed a higher-frequency vibrational mode than did aragonite [21, 22].

Figure 3 shows the LIBS spectra of the $CaCO_3$ polymorphs. Aragonite and calcite show almost the same peaks for calcium, because two polymorphs have the same

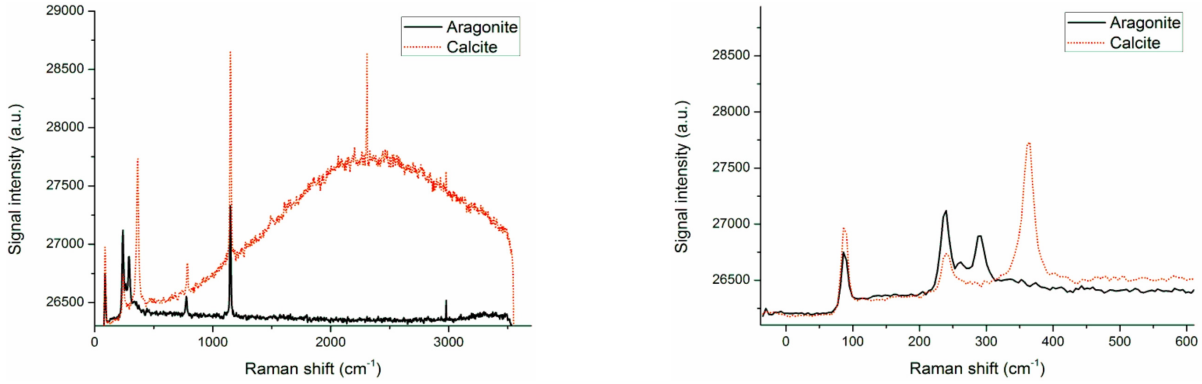

FIG. 2. (a) Raman shift of the $CaCO_3$ polymorphs, and (b) signal difference around 100-400 cm^{-1}.

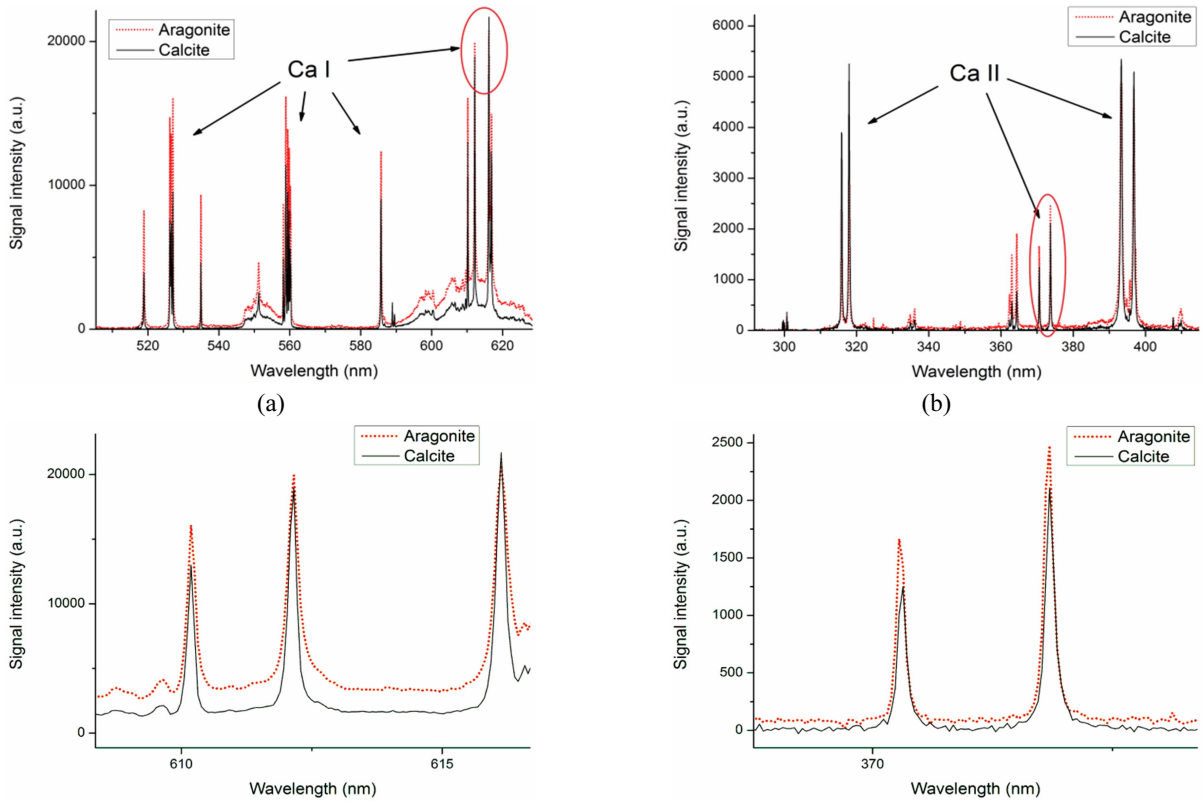

FIG. 3. LIBS signals of the $CaCO_3$ polymorphs: (a) neutral atom; (b) singly ionized atom; (c) 5s → 4p transition of neutral atom; (d) 5s → 4p transition of singly ionized atom.

composition and only differ in crystal structure. Signals for neutral calcium (Ca I) are detected in a range around 530-600 nm, whereas signals for singly ionized calcium (Ca II) appear in a range around 310-400 nm. As shown in Figs. 3(a) and 3(b), aragonite's signal intensities were generally higher than calcite's for neutral calcium (Ca I), whereas calcite showed stronger signals for singly ionized calcium (Ca II). Moreover, some of the peaks circled in Figs. 3(a) and 3(b) showed a reversal of the general tendency. These specific peaks are depicted in Figs. 3(c) and 3(d) and highlight the wavelengths 612.2 nm and 616.2 nm for Ca I, and 370.5 nm and 373.7 nm for Ca II.

Different signal intensities and intensity conversion between aragonite and calcite occurred, due to the electronic interaction in plasma and electronic transition in atoms or ions. Here, maximum signal intensity is used without background subtraction.

3.1.1. Ca I Behavior in Plasma

Generally, the intensity of the aragonite signal overwhelms the calcite signal at almost all wavelengths in LIBS. As shown in Table 1, the molecular density of aragonite is higher than that of calcite; therefore, aragonite contains considerably more Ca^{2+} and CO_3^{2-} ions in the laser beam's spot than does calcite [23]. In addition, when molecular components in $CaCO_3$ are irradiated by a laser beam, plasma containing ionized or atomic elements such as Ca, C, and O is generated. Therefore, aragonite generates a larger number of Ca atoms and electrons than calcite, which allows the interaction between electrons and Ca atoms to be more frequent. As a result, Ca I of aragonite has a higher signal intensity, due to its higher density (number of molecules in the unit-cell volume).

At wavelengths of 612.2 nm and 616.2 nm, which correspond to the $5s \rightarrow 4p$ orbital transition, the calcite signal was stronger than that of aragonite. This signal inversion is mainly due to the different molecular density of the two polymorphs.

First, each Ca^{2+} ion in aragonite is combined with four CO_3^{2-} ions, whereas Ca^{2+} in calcite is connected to three CO_3^{2-} ions [26]. Furthermore, it is well known that the structure of calcite features sixfold coordination of Ca^{2+}, while aragonite is formed with ninefold coordination, spatially in three-dimensional (3D) coordinates. To find structural stability, aragonite structurally transforms to calcite at around 600 K, before it is ionized [23, 27-29]. Especially in [29] this transformation occurred rapidly above 698 K. Therefore, the increasing quantity of Ca I during the transformation from aragonite to calcite is one of the factors behind signal inversion, because the number of electrons in the unit-cell volume of aragonite that can interact with protons in Ca ions or atoms are also decreased.

Second, for the electrons in aragonite, it is difficult to find stability in the plasma. As shown in Table 1, the quantity of electrons generated during the ablation process is largely dependent on molecular density. In addition, the electron density in the unit-cell volume is larger for aragonite than calcite, whereas its molecular volume is small. Therefore, the interaction of atomic or ionic components in aragonite occurs much more frequently than in calcite, in plasma [22].

Third, the largest energy gap for an electronic transition between Ca I energy levels is for $4s4p\ ^3P^0$ to $4s5s\ ^3S$ (Table 2). This means that it is time-consuming and difficult to transit from 5s to the stable 4p state in extreme conditions such as plasma. Because stable calcite has fewer molecular bonds than aragonite, all bonds are rapidly disconnected, compared to the bonds in aragonite.

Therefore, aragonite is still in the process of breaking and rearranging molecular structures when Ca atoms in calcite are already attracting electrons. In other words, aragonite, with its less stable structure and higher molecular density, consumes more energy through bond disconnection, unit-cell expansion and heat transfer as it forms a more stable structure. Therefore, aragonite is still in the process of breaking and rearranging its bonds while Ca atoms in calcite are already attracting electrons. Stable calcite does not need to consume energy for these processes, which helps to explain the signal inversion.

Also, in the aragonite sample a large quantity of trigonal CO_3^{2-} ions repel the electrons during the process of rearranging its structure. This is because CO_3^{2-} ions are composed of covalent bonds, which are not disassociated easily compared to ionic bonds. In [27], simulation showed

TABLE 1. Properties of the $CaCO_3$ polymorphs aragonite and calcite [24, 25]

	Calcite	Aragonite
Chemical formula	$CaCO_3$	$CaCO_3$
Unit cell volume	367.85 Å^3	226.17 Å^3
Density	2.71 g/cm^3	2.93 g/cm^3
Crystal system	Rhombohedral	Orthorhombic
Hardness	3	3.5 - 4
Electron density	2.71 g/cm3	2.93 g/cm^3
Photoelectric ($U = PE \times \rho_{electron}$)	$PE_{calcite}$ = 5.06 barns/electron U = 13.70 barns/cm^3	$PE_{aragonite}$ = 5.06 barns/electron U = 14.81 barns/cm^3

TABLE 2. Orbital transition energies of Ca I and Ca II [30]

Ca I			Ca II		
Configuration	Term	Energy level (cm^{-1})	Configuration	Term	Energy level (cm^{-1})
$4s^2$	^1S	0	4s	^2S	0
4s4p	$^3P^0$	15157.901	3d	^2D	13650.20
3d4s	^3D	20335.360	4p	$^2P^0$	25191.518
3d4s	^1D	21849.634	5s	^2S	52166.94
4s4p	$^1P^0$	23652.304	4d	^2D	56839.26
4s5s	^3S	31539.495	5p	$^2P^0$	60533.03
4s5s	^1S	33317.264	4f	$^2F^0$	68056.92
3d4p	$^3F^0$	35730.454	6s	^2S	70677.63
3d4p	$^1D^0$	35835.413			
4s5p	$^3P^0$	36547.688			
4s5p	$^1P^0$	36731.615			
4s4d	^1D	37298.287			
4s4d	^3D	37748.197			
3d4p	$^3D^0$	38192.392			
$4p^2$	^3P	38417.543			
Ca II (limit)	$^2S_{1/2}$	49305.95	Ca III (limit)	$^1S_0$	95751.88

that all CO_3^{2-} ions are disordered at 1938 K. This also contributes to reducing the interactions between electrons and Ca^{2+} ions or Ca atoms in aragonite. Furthermore, the increase in the unit-cell volume of aragonite causes a decrease in its electron density. These factors concerning energy consumption for rearrangement and repulsive force in molecular structures can increase the signal for calcite, contrary to decreasing the signal for aragonite.

Until now we have mainly discussed the different molecular densities of polymorphs as a factor for signal inversion of Ca I in calcite.

In general, the inversion of signal intensity does not always occur in all molecular samples. For example, our other results involving $CaSO_4$ did not show large inversion of signals, but did show small changes in signal intensity. These intensity differences depend mostly on the quantity of electrons in the plasma. For this reason, we need to focus on the specific wavelength area that shows the smallest changes of signal intensity between two polymorphs, rather than on the inversion of signals. The areas of 612.2 nm and 616.2 nm that show the smallest changes of signal intensity correspond to the 4s5s triplet - 4s4p triplet transition.

When electrons exist in a 4s5s triplet state, they can transit to the 4s4p triplet, 4s3d triplet, and 4s3d singlet states. In addition, the possible transition route can be selected based on the selection rules. Following the selection rules for electric dipole transitions, some transition routes between the 4s4p triplet, 4s3d triplet, and 4s3d singlet states are forbidden. Therefore, electrons in the 4s5s triplet state can transit only to a 4snp state, except for the 4snd state, regardless of the principal quantum number n. In other words, the probability of a 4s5s triplet to 4s3d orbital transition is very low, although the 3d singlet and 3d triplet states are at a higher, metastable energy level than the 4s4p orbital. Therefore the 4s5s triplet - 4s4p triplet transition dominates.

3.1.2. Ca II Behavior in Plasma

Generally, the signal intensity of Ca II in calcite was larger than that in aragonite, at almost all wavelengths, unlike in the Ca I case (Fig. 3(b)). Also, it is well known that Ca^{2+} ions in calcite combine with relatively smaller quantities of CO_3^{2-} than in aragonite [26]. Therefore, calcite has a stable molecular structure in its unit-cell volume, and its molecular structure does not need to be rearranged, unlike the case of aragonite. Therefore, when calcite is irradiated with a laser beam, all of the weak ionic bonds between the Ca^{2+} and CO_3^{2-} ions can easily be disconnected, whereas in aragonite, expanding and rearranging its molecular structure is initially time-consuming [22].

After dissociation of ionic bonds, the Ca^{2+} cation begins to attract electrons from the plasma. The doubly ionized calcium cations easily recombine with electrons to form Ca II. However, some factors interrupt the recombination of Ca^{2+} and electrons in the plasma. First, repulsive inter-

actions between components in calcite occur less frequently than in aragonite, due to the large molecular density of aragonite. Therefore, the signal intensity of Ca II in calcite is higher than that in aragonite plasma. The second factor is the electronegativity of components in the $CaCO_3$ polymorphs. Especially as aragonite has a greater concentration of electrons and of C and O atoms in its plasma, aragonite loses more electrons than calcite to the N and O atoms in ambient air, which have large electronegativity. Also, N needs three electrons to satisfy the Octet Rule, whereas O requires only two electrons. Therefore, electronegativity can influence the higher signal of Ca II in calcite than in aragonite.

However, the special signal intensity at 370.5 nm and 373.7 nm, which corresponds to the 5s → 4p orbital transition, showed an inversion, as seen in Fig. 3(d), in which aragonite signals were higher than those of calcite.

First, as shown in Table 1, the electron density of aragonite is greater than that of calcite. Hence, the electrons in plasma from aragonite are more abundant than in plasma from calcite. Second, when electrons in a 5s doublet lose their energy, they can select the transition routes to the 3d doublet or 4p doublet states, which are well known for metastable conditions near the ground state $[Ar]4s^1$. We therefore can infer that almost all electrons that transit from the 5s doublet follow the 4p doublet - 4s doublet transition route.

Therefore, the signal inversion for aragonite in Ca II can be explained by two processes. First, the signal inversion is due to the different quantities of electrons in plasma. Second, the electronic transition from 5s doublet to 4p doublet can explain why signal inversion must appear at 370.5 nm and 373.7 nm especially.

Particularly, it must be emphasized that the reader needs to focus more on small variations in signal intensities than on signal inversion, to make a generalized standard for classifying polymorphs using LIBS.

3.2. Gypsum and Anhydrite Samples (Based on $CaSO_4$)

Figure 4 shows the Raman signals of gypsum and anhydrite samples. Peaks due to SO_4^{2-} ions can be detected at similar ranges of wave numbers, around 1026 cm^{-1}, which implies an internal mode. However, several different signals are detected below 1000 cm^{-1}, especially in the 600-800 cm^{-1} range. In addition, partial signals of gypsum were observed at around 3400 cm^{-1}, which indicates modes in the O-H stretching region, implying the presence of H_2O. However, anhydrite did not show signals for H_2O, since it is an anhydrous mineral. These differences in Raman signals also resulted from the different molecular densities of gypsum and anhydrite samples. In Table 3 anhydrite is shown to have a larger molecular density than gypsum, whereas its unit-cell volume is relatively small.

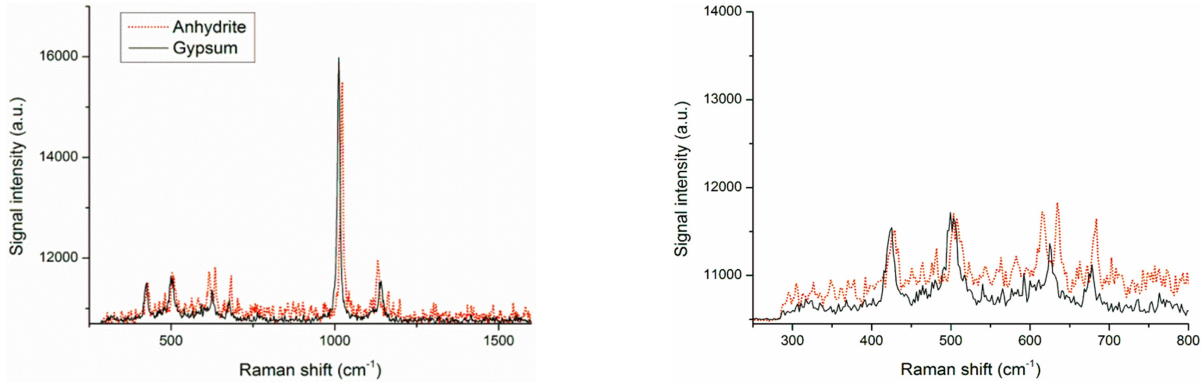

(a) (b)

FIG. 4. (a) Raman shift of the gypsum and anhydrite samples, and (b) signal difference around 200-800 cm^{-1}.

TABLE 3. Properties of gypsum and anhydrite (based on $CaSO_4$) [24, 25]

	Gypsum	Anhydrite
Chemical formula	$CaSO_4 \cdot 2H_2O$	$CaSO_4$
Unit cell volume	495.15 $Å^3$	305.48 $Å^3$
Density	2.3 g/cm^3	2.97 g/cm^3
Crystal system	Monoclinic	Orthorhombic
Hardness	2	3 - 3.5
Electron density	2.36 g/cm^3	2.97 g/cm^3
Photoelectric ($U= PE \times \rho_{electron}$)	PE_{gypsum} = 3.97 barns/electron U = 9.37 barns/cm^3	$PE_{anhydrite}$ = 5.03 barns/electron U = 14.93 barns/cm^3

Similarly, gypsum and anhydrite can also be analyzed using Raman spectroscopy due to their different molecular properties, as analyzed for the $CaCO_3$ case above [1].

Figure 5 shows the LIBS signals of the neutral atoms (Ca I) and singly ionized ions (Ca II) in gypsum and anhydrite plasma. Similar to the $CaCO_3$ case, differences in signal intensity can be observed for Ca I and Ca II in all the images in Fig. 5.

For Ca I, the signal for anhydrite was larger than that for gypsum in almost all of the wavelength ranges, except for the specific site, which shows a small signal gap at 612.2 nm and 616.2 nm. In contrast, for Ca II, the gypsum signal overwhelms the anhydrite signal in almost all ranges, whereas the small gaps in signal intensities of the two samples are shown at 370.5 nm and 373.7 nm especially.

As previously emphasized, inversion of signal intensity is not important. Although the differences in signal intensity for gypsum and anhydrite are smaller than for $CaCO_3$ polymorphs, samples can still be classified using generalized standard wavelengths (5s - 4p transition). Because the small differences in signal intensities occurred, certain other areas also correspond to the 5s to 4p transition of electron in the gypsum and anhydrite case.

The different molecular densities of gypsum and anhydrite are mainly due to the existence of H_2O molecules. First, gypsum has weak hydrogen bonds between the H_2O molecules and SO_4^{2-} ions in its structure, which yields a small molecular density. On the other hand, anhydrite does not contain a hydrogen layer, due to its anhydration effect, which induces a denser structure than in gypsum. Therefore, anhydrite has an orthorombic structure, in which eight SO_4^{2-} ions surround one Ca^{2+} ion. In addition, stable gypsum tends to dehydrate by absorbing heat, as shown in the following reversible reaction equation $CaSO_4 \cdot 2H_2O(gypsum) \rightarrow CaSO_4(anhydrite) + H_2O$.

Also, the reverse reaction, in which anhydrite is transformed to gypsum, mainly occurs due to the attractive force between the electrically polarized H_2O and SO_4^{2-} ions [31, 32].

In the case of Ca I, the strong intensities for anhydrite at almost all wavelengths is mainly due to its large molecular density. This is because statistically more of the Ca^{2+} ions in dense anhydrite are irradiated by the laser beam. In addition, slight signal inversion for gypsum occurs, especially at 612.2 nm and 616.2 nm. This can be analyzed in the same way as in the $CaCO_3$ case, which showed a high energy consumption needed to rearrange its structure, repulsive interactions between components, and hard transition of electrons due to a large energy gap.

In addition, in the Ca II case, factors such as deprivation of electrons by N and O in ambient air, small differences in effective nuclear charge, and multiple repulsive forces of SO_4^{2-} ions could lead to a small gap in signal intensities

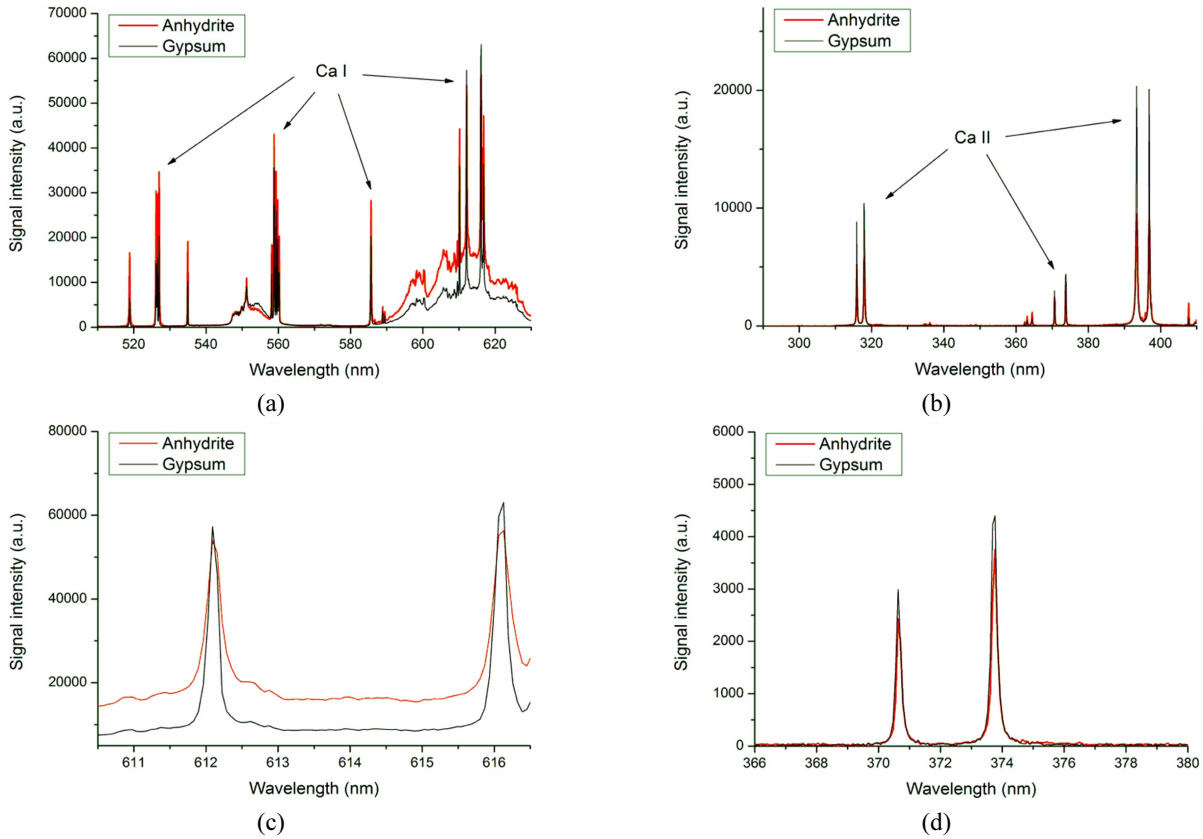

FIG. 5. LIBS signals of gypsum and anhydrite samples: (a) neutral atom; (b) singly ionized atom; (c) 5s → 4p transition of neutral atom; (d) 5s → 4p transition of singly ionized atom.

of the two samples, as stated above in the analysis of $CaCO_3$. In short, the differences in molecular density dominated and induced small intervals of signal intensities in the case of gypsum and anhydrite case, similar to the case of $CaCO_3$ polymorphs. However, the other differences between the $CaCO_3$ and $CaSO_4$ cases still need to be considered. Focusing on the fact that signal inversion is not clearly shown in the $CaSO_4$ case, we can compare the factors influencing the quantity of electrons in the $CaCO_3$ and $CaSO_4$ plasmas. The first factor is the presence of H_2O. The different densities of the two samples (gypsum and anhydrite) were due to the presence of H_2O in one structure, whereas the stability of $CaCO_3$ polymorphs is determined only by the molecular arrangement. Therefore, the number of electrons in the $CaSO_4$ plasma is lower than that in the $CaCO_3$ case, because either the induced dipole moment of H_2O attracts electrons, or the O^{2-} ions in the H_2O apply a repulsive force to the electrons in the plasma.

Second, the SO_4^{2-} in $CaSO_4$ makes a larger repulsive force than $CaCO_3$ towards electrons in plasma. This is because the tetrahedral structure of SO_4^{2-} can apply a repulsive force to larger regions of space than can the trigonal planar structure of CO_3^{2-}. In addition, the absolute number of O^{2-} ions is more abundant in $CaSO_4$. Furthermore, the larger ionic size of SO_4^{2-} than CO_3^{2-} can create a denser, less stable plasma. This is because SO_4^{2-} ions experience a stronger repulsive force from N and O in ambient air, which interferes with the electronic transition to a stable energy level. Therefore, the reduced quantity of electrons in $CaSO_4$ plasma yields smaller signals than $CaCO_3$ plasma does.

3.3. Signal Ratio Comparison of Samples

Table 4 shows the signal intensity ratios of the two polymorphs. The signal intensity ratio was obtained by dividing the intensities for the two samples. Also, we compared the signals from the 5s - 4p transition route to those from the other routes. Other transition routes in Ca I (527.0 nm and 585.7 nm) and Ca II (315.9 nm and 373.7) are selected. Because they are the main peaks of Ca I, II near 5s - 4p wavelengths, which follows the other transition routes. We intend to demonstrate that these routes show distinct intensity ratios, compared to the 5s - 4p routes. For Ca I of the $CaCO_3$ polymorphs, the wavelength of 616.2 nm ($5s \rightarrow 4p$) showed a lower relative intensity ratio (0.96) than those of the 527.0 nm ($4p \rightarrow 4s$) and 585.7 nm ($4p^2 \rightarrow 4s4p$) signals (1.67 and 1.35 respectively). In addition, the value of the intensity ratio at 616.2 nm did not exceed 1. In contrast, for Ca II of the $CaCO_3$ polymorphs, the wavelength of 373.7 nm showed a higher relative intensity ratio (1.17) than other signals, which showed ratios smaller than 1. In addition, in the gypsum and anhydrite samples, special relative intensity ratios were shown at the same wavelengths of 373.7 nm and 616.2 nm. In short, the wavelengths of 373.7 nm and 616.2 nm that correspond to the electronic transition between the 5s and 4p states in Ca showed special intensity ratios near 1. Therefore, when we need to classify polymorphs that are based on Ca, we can select standard wavelengths such as 373.7 nm and 616.2 nm in LIBS analysis.

It is especially significant that 373.7 nm for Ca II in the gypsum and anhydrite samples showed the largest value (0.85), although ratio values over 1 cannot be found for any wavelengths. However, the comparison of relative signal intensity ratios for classifying polymorphs is still reasonable, though the signal inversion is not shown numerically, because the small signal intensity ratios that appeared at the special wavelengths of 373.7 nm and 616.2 nm follow the selection rules in Ca atoms or ions. In contrast, the signal inversion is caused mainly by the interactions of electrons in the plasma. This is why we analyzed the factors for classifying polymorphs in two parts, interactions between components of polymorphs and electronic transition in atoms. In addition, if the signal intensity ratio is near 1, the transition possibility does not change much, which means that many electrons transit to the metastable state near the ground state. In other words, if the signal ratio values are near 1, the electrons in the 5s state transit to the metastable 4p state more frequently than to any other, less stable states. In addition, we can only assume that the larger influence of SO_4^{2-} ions resulted in almost a small signal intensity gap and ratio than the CO_3^{2-} ions in $CaCO_3$, as stated in the above chapter. Therefore, the reason for the small signal ratio of less than 1

TABLE 4. Relative comparisons of LIBS signal intensities of $CaCO_3$ polymorphs and gypsum and anhydrite samples

Signals (nm)	Ca I (Neutral atom signals)			Ca II (Singly ionized ion signals)		
	527.0 ($3d4p \rightarrow 3d4s$)	585.7 ($4p2 \rightarrow 4s4p$)	616.2 ($4s5s \rightarrow 4s4p$)	315.9 ($4d \rightarrow 4p$)	373.7 ($5s \rightarrow 4p$)	393.4 ($4p \rightarrow 4s$)
Calcite	9535	9053	21691	3899	2110	5345
Aragonite	16085	12256	20721	2626	2478	4471
Ratio (A/C)	1.67	1.35	0.96	0.67	1.17	0.84
Gypsum	20399	20244	63037	8808	4397	20342
Anhydrite	34646	28246	56310	5186	3759	7888
Ratio (A/G)	1.70	1.40	0.89	0.59	0.85	0.39

for gypsum and anhydrite samples could be the influence of SO_4^{2-} ions that are related to the interactions of elements in the $CaSO_4$ plasma.

In conclusion, the electronic transition from 5s to 4p can become a standard point, because both samples are based on Ca atoms or ions in our study. In addition, it should be recalled that the absolute value of the ratio for the 5s - 4p transition is not important. Only the existence of the special wavelengths themselves, which show signal inversions or the smallest gap of signal intensities, is sufficient to classify polymorphs by physical principles in atoms.

IV. CONCLUSION

Classification of samples (based on $CaCO_3$ and $CaSO_4$) was performed using LIBS, which is known for providing only atomic or ionic information. In both cases of $CaCO_3$ polymorphs and gypsum and anhydrite, the wavelength corresponding to the 5s - 4p orbital transition showed a special signal intensity ratio, compared to other wavelengths. For example, the calcite signal is higher than the aragonite signal especially at 612.2 nm and 616.2 nm for Ca I, whereas the aragonite signal is higher than the calcite signal at 370.5 nm and 373.7 nm for Ca II. In contrast, gypsum and anhydrite showed slight signal inversion, which could be analyzed in the same way as in the $CaCO_3$ case. The differences between the two samples are mostly due to the gap in the size of the signal intensities, influenced by the SO_4^{2-} ions (which have a stronger repulsive force) and the large size of the molecule.

This can be explained mainly by two factors: the interactions of components in the $CaCO_3$ and $CaSO_4$ plasmas, and the process of electronic transition in the atoms or ions. This is because specially selected wavelengths are related to the electronic transition, whereas signal intensity is only dominated by interactions and different densities of components such as electrons, atoms, and ions in plasma.

In addition, by examining the ratios of signal intensities, we recognized that the special wavelength peaks showed different values compared to the other signals. If the signal intensity ratio approaches 1, we can say that all peripheral electrons completely transited to the 5s to 4p metastable state, because the probability of transition to the metastable state changes less than any other transition route. In addition, selection rules follow the dominant electric dipole transition that determines transition routes. Therefore, the 5s - 4p transition in the Ca atoms or ions can be a generalized standard for classifying polymorphs.

In conclusion, based on the above principles of plasma and electronic transition, we can obtain molecular information as well as ionic or atomic signals, enabling the classification of polymorphs using LIBS.

These advantages of LIBS will maximize the utilization of the complementary combined LIBS-Raman system. By using this system, the accuracy of classifying polymorphs can be improved, since the polymorphs classification data from LIBS can be reexamined using Raman spectroscopy.

ACKNOWLEDGMENT

The authors wish to acknowledge financial support from the Korea National Research Foundation under the National Space Laboratory Program 2014 (NRF-014M1A3A3A0203 4903) through the IAAT at Seoul National University.

REFERENCES

1. N. Prieto-Taboada, O. Gómez-Laserna, I. Martínez-Arkarazo, M. Á. Olazabal, and J. M. Madariaga, "Raman spectra of the different phases in the $CaSO_4$-H_2O system," Anal. Chem. **86**(20), 10131-10137 (2014).
2. M. D. Dyar, E. Breves, E. Jawin, G. Marchand, M. Nelms, V. O'Connor, S. Peel, Y. Rothstein, E. C. Sklute, and M. D. Lane, "What lurks in the martian rocks and soil? investigations of sulfates, phosphates, and perchlorates. Mössbauer parameters of iron in sulfate minerals," Am. Mineral. **98** (11-12), 1943-1965 (2013).
3. K. Melessanaki, M. Mateo, S. C. Ferrence, P. P. Betancourt, and D. Anglos, "The application of LIBS for the analysis of archaeological ceramic and metal artifacts," Appl. Surf. Sci. **197**, 156-163 (2002).
4. F. C. D. Lucia, R. S. Harmon, K. L. McNesby, R. J. Winkel, and A. W. Miziolek, "Laser-induced breakdown spectroscopy analysis of energetic materials," Appl. Opt. **42**(30), 6148-6152 (2003).
5. A. K. Knight, N. L. Scherbarth, D. A. Cremers, and M. J. Ferris, "Characterization of Laser-Induced Breakdown Spectroscopy (LIBS) for application to space exploration," Appl. Spectrosc. **54**(3), 331-340 (2000).
6. F. Rull, J. Martinez-Frias, A. Sansano, J. Medina, and H. G. M. Edwards, "Comparative micro-Raman study of the Nakhla and Vaca Muerta meteorites," J. Raman Spectrosc. **35**(6), 497-503 (2004).
7. A. Wang, J. J. Freeman, B. L. Jolliff, and I.-M. Chou, "Sulfates on Mars: A systematic Raman spectroscopic study of hydration states of magnesium sulfates," Geochim. Cosmochim. Acta **70**(24), 6118-6135 (2006).
8. R. J. Hemley, "Pressure dependence of Raman spectra of SiO_2 Polymorphs: α-quartz, coesite, and stishovite," High-Pressure Res. Miner. Phys. **347** (1987).
9. M. Hoehse, D. Mory, S. Florek, F. Weritz, I. Gornushkin, and U. Panne, "A combined laser-induced breakdown and Raman spectroscopy Echelle system for elemental and molecular microanalysis," Spectrochim. Acta Part B: At. Spectrosc. **64**(11), 1219-1227 (2009).
10. R. Bruder, V. Detalle, and C. Coupry, "An example of the complementarity of laser-induced breakdown spectroscopy and Raman microscopy for wall painting pigments analysis," J. Raman Spectrosc. **38**(7), 909-915 (2007).
11. A. Giakoumaki, I. Osticioli, and D. Anglos, "Spectroscopic analysis using a hybrid LIBS-Raman system," Appl. Phys. A

83(4), 537-541 (2006).
12. J. Moros, J. A. Lorenzo, P. Lucena, L. M. Tobaria, J. J. Laserna, "Simultaneous Raman spectroscopy-laser-induced breakdown spectroscopy for instant standoff analysis of explosives using a mobile integrated sensor platform," Anal. Chem. **82**(4), 1389-1400 (2010).
13. J. Moros, J. A. Lorenzo, and J. J. Laserna, "Standoff detection of explosives: critical comparison for ensuing options on Raman spectroscopy-LIBS sensor fusion," Anal. Bioanal. Chem. **400**(10), 3353-3365 (2011).
14. S. K. Sharma, A. K. Misra, P. G. Lucey, R. C. Wiens, and S. M. Clegg, "Combined remote LIBS and Raman spectroscopy at 8.6 m of sulfur-containing minerals, and minerals coated with hematite or covered with basaltic dust," Spectrochim. Acta Part A: Mol. Biomol. Spectrosc. **68**(4), 1036-1045 (2007).
15. G. B. Courreges-Lacoste, B. Ahlers, and F. R. Pérez, "Combined Raman spectrometer/laser-induced breakdown spectrometer for the next ESA mission to Mars," Spectrochim. Acta Part A: Mol. Biomol. Spectrosc. **68**(4), 1023-1028 (2007).
16. A. Frebel, J. E. Norris, W. Aoki, S. Honda, M. S. Bessell, M. Takada-Hidai, T. C. Beers, and N. Christlieb, "Chemical abundance analysis of the extremely metal-poor star HE 1300 + 0157," Astrophys. J. **658**(1), 534-552 (2007).
17. R. Cayrel, E. Depagne, M. Spite, V. Hill, F. Spite, P. François, B. Plez, T. Beers, F. Primas, J. Andersen, B. Barbuy, P. Bonifacio, P. Molaro, and B. Nordström, "First stars V - Abundance patterns from C to Zn and supernova yields in the early Galaxy," Astron. Astrophys. **416**(3), 1117-1138 (2004).
18. B Emmoth, M. Braun, J. Bromander, and I. Martinson, "Lifetimes of excited levels in Ca I - Ca III," Phys. Scr. **12**(1-2), 75-79 (1975).
19. J. E. Stalnaker, Y. L. Coq, T. M. Fortier, S. A. Diddams, C. W. Oates, and L. Hollberg, "Measurement of excited-state transitions in cold calcium atoms by direct femtosecond frequency-comb spectroscopy," Phys. Rev. A **75**(4), 040502 (2007).
20. L. Pasternack, D. R. Yarkony, P. J. Dagdigian, and D. M. Silver, "Experimental and theoretical study of the Ca I 4s3d ^{1}D-4s2 ^{1}S and 4s4p ^{3}P1-4s^{2} 1S forbidden transitions," J. Phys. B: At. Mol. Phys. **13**(11), 2231-2241 (1980).
21. N. H. D. Leeuw and S. C. Parker, "Surface structure and morphology of calcium carbonate polymorphs calcite, aragonite, and vaterite: an atomistic approach," J. Phys. Chem. B **102** (16), 2914-2922 (1998).
22. A. Pavese, M. Catti, G. D. Price, and R. A. Jackson, "Interatomic potentials for CaCO3 polymorphs (calcite and aragonite), fitted to elastic and vibrational data," Phys. Chem. of Miner. **19**(2), 80-87 (1992).
23. B. Xu and K. M. Poduska, "Linking crystal structure with temperature-sensitive vibrational modes in calcium carbonate minerals," Phys. Chem. Chem. Phys. **16**(33), 17634-17639 (2014).
24. David Barthelmy (http://webmineral.com/, (1997-2014).
25. Hudson Institute of Mineralogy (http://www.mindat.org/), (1993-2015).
26. The University of Liverpool (http://www.chemtube3d.com/solidstate/SS-CaCO3.htm), (2008-2015).
27. J. Liu, M. M. Ossowski, J. R. Hardy, C. Duan, and W. N. Mei, "Simulation of structural transformation in aragonite $CaCO_3$," AIP Conference Proceedings, 2000.
28. F. M. Hossain, G. E. Murch, I. V. Belova, and B. D. Turner, "Electronic, optical and bonding properties of $CaCO_3$ calcite," Solid State Commun. **149**(29), 1201-1203 (2009).
29. J. Perić, M. Vučak, R. Krstulović, L. Brečević, and D. Kralj, "Phase transformation of calcium carbonate polymorphs," Thermochim. Acta **277**, 175-186 (1996).
30. NIST (http://physics.nist.gov/PhysRefData/Handbook/Tables/calciumtable5.htm), (2010-2015).
31. E. S. A. Seif, "Geotechnical characteristics of anhydrite/gypsum transformation in the middle miocene evaporites, red sea coast, Egypt," Arabian J. Sci. Eng. **39**(1), 247-260 (2014).
32. G. Azimi and V. G. Papangelakis, "Mechanism and kinetics of gypsum-anhydrite transformation in aqueous electrolyte solutions," Hydrometallurgy **108**(1), 122-129 (2011).